

Controlling Tin Halide Perovskite Crystallization by Blade Coating Toward Reproducible and Efficient Solar Cells

Lijun Chen, Lorenzo Di Mario, Giuseppe Portale, Christoph J Brabec, and Maria Antonietta Loi*

Tin-based perovskites have shown significant potential for photovoltaics applications due to their reduced toxicity and ideal bandgap when compared with the Pb counterpart. However, the utilization of industry-compatible and scalable fabrication techniques has remained limited to date, due to the unique crystallization properties of tin-based perovskites. Here, tin perovskite solar cells prepared using a two-step blade coating process is reported. The broad exploration of the space of parameters and the corresponding crystallization control mechanisms showed that waiting time and solvent nature are equally important as coating speed and coating temperature in enhancing the quality of tin(II) iodide films deposited in the first step and the subsequent conversion in the second step. Highly reproducible and efficient tin-based devices are achieved, exhibiting a maximum power conversion efficiency (PCE) of 10.7% and an impressive fill factor (FF) of 79%. To the knowledge, these values are among the highest reported thus far using a scalable technique. Additionally, it is important to notice that the devices retain over 90% of the initial PCE over 4 months in an inert atmosphere and exhibit good operational stability. The results demonstrate a clear roadmap towards fabricating tin perovskite devices with industry-compatible techniques.

1. Introduction

Perovskite solar cells (PSCs) are highly promising candidates for future photovoltaic technologies with low-cost fabrication and high device efficiency. Nevertheless, their exceptional optoelectronic properties are typically achieved using lead-based compounds, raising significant environmental concerns regarding their massive exploitation.^[1] Tin (Sn) perovskite emerges as one of the most promising lead (Pb)-free alternatives owing to its ideal band gap, closely approaching the Shockley-Queisser limit (1.3–1.4 eV),^[2,3] along with its high carrier mobility.^[4–8] However, the properties of tin perovskites present new challenges.^[9–11] Such as low defect tolerance,^[12,13] rapid crystallization,^[14] and oxidative instability.^[15–18] The extensive efforts made by the research community over the past 10 years have yielded promising results, particularly through the incorporation of

varying amounts of bulkier organic cations, with the highest recorded efficiency reaching up to 17.13%.^[6,10,19,20]

It is noteworthy that the majority of these high-efficiency tin-based devices and modules are fabricated using spin coating.^[21–23] Unfortunately, spin coating has several limitations when thinking to possible scalability, substrate dimension, cost, deposition speed, and yield are only a few of them. Blade coating instead, is considered as one of the most promising techniques for scalable fabrication of PSCs, and it is recognized that procedures developed with blade coating can be transferred to industrial scale techniques such as Roll-to-Roll, slot die coating, and other similar techniques.^[24] Recently, an 8-cell interconnected mini module based on tin was fabricated and achieved a PCE of 5.7%,^[25] while this result is encouraging, it is still far from efficiency values expected for commercialization. In particular in this experiment, the FF decreases significantly increasing the cell area due to the difficulty in controlling the crystallization process during the blade coating and the resulting inhomogeneity of the tin perovskite films.^[26]

Blade coating involves the formation of a meniscus-shaped liquid edge of precursor solutions, which is spread to form a liquid film on a substrate. The difference of surface tension between the substrate and the liquid precursors can lead to the

L. Chen, L. D. Mario, G. Portale, C. J Brabec, M. A. Loi
Zernike Institute for Advanced Materials
University of Groningen
Nijenborgh 4, Groningen 9747 AG, The Netherlands
E-mail: M.A.Loi@rug.nl

L. Chen, M. A. Loi
CogniGron (Groningen Cognitive Systems and Materials Center)
University of Groningen
Nijenborgh 4, Groningen 9747 AG, The Netherlands

C. J Brabec
Institute of Materials for Electronics and Energy Technology (i-MEET)
Friedrich-Alexander-University Erlangen-Nürnberg
Martensstrasse 7, 91058 Erlangen, Germany

C. J Brabec
Helmholtz-Institute Erlangen-Nürnberg (HI ERN)
Immerwahrstraße 2, 91058 Erlangen, Germany

 The ORCID identification number(s) for the author(s) of this article can be found under <https://doi.org/10.1002/aenm.202503611>

© 2025 The Author(s). Advanced Energy Materials published by Wiley-VCH GmbH. This is an open access article under the terms of the [Creative Commons Attribution-NonCommercial-NoDerivs](#) License, which permits use and distribution in any medium, provided the original work is properly cited, the use is non-commercial and no modifications or adaptations are made.

DOI: 10.1002/aenm.202503611

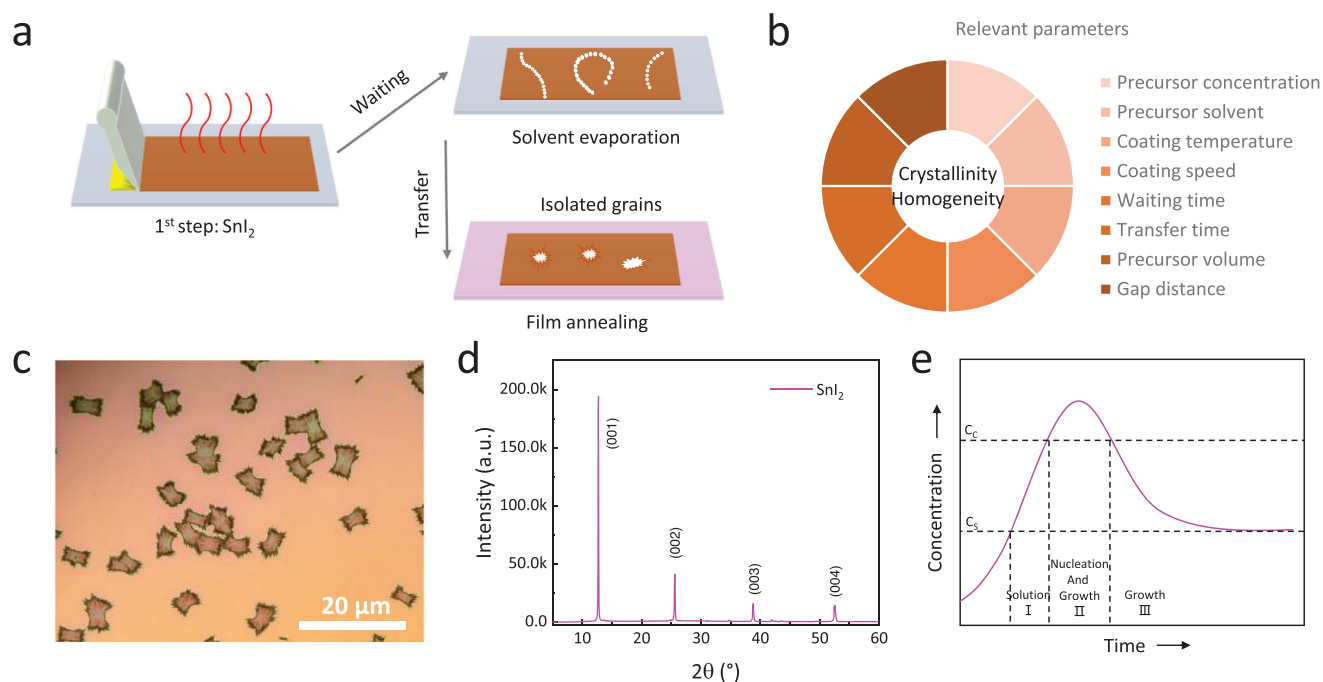


Figure 1. Effect of 1st step deposition on film crystallinity and homogeneity. a) Schematic diagram of the deposition of SnI₂ film with blade coating (first step). b) Relevant parameters that influence the crystallinity and homogeneity of films. c) Optical microscopic image of SnI₂ film deposited at room temperature and high coating speed. d) XRD pattern of SnI₂ film processed with optimized coating conditions. e) The Lar Mer model for nucleation and growth of SnI₂ thin films. C_c, critical concentration; C_s, saturation concentration.

formation of a coffee-ring-like film during the drying of the perovskite solution.^[27] The control of the nucleation and crystal growth processes to achieve dense and uniform films (avoiding the coffee-ring effect) through natural drying is very challenging. Several physical (gas quenching, hot casting, and vacuum treatment) and chemical (solvent engineering,^[28] interfacial engineering, etc.) strategies were proposed to optimize the nucleation rate, the grain size, and consequently film morphology.^[29,30]

While for Pb perovskite the conversion mechanism and advanced engineering strategies for the two-step blade coating fabrication process have been reported, not much was done on other compositions.^[31,32] Recently, we reported a heat-assisted two-step blade coating process for Pb-Sn perovskite films.^[33] However, undesired crystal orientations and the presence of unreacted PbI₂/SnI₂ are key factors that degrade device performance. The situation for pure Sn perovskite is even more complicated, as the crystallization process is markedly different from the one of Pb and Pb-Sn alloys, due in particular to the different solubility of Pb and Sn ions.^[34] Therefore, to fabricate reproducible Sn-perovskite devices utilizing scalable deposition methods, a careful optimization of the process should be performed.

In this study, we explore the space of parameters for obtaining high quality crystalline Sn-based perovskite films by a two-step blade coating deposition method. We identify the most influential parameters to be the coating temperature and speed, waiting time, and the solvent nature. Both the quality of the SnI₂ film deposited in the first step and the subsequent conversion process in the second step significantly influence device efficiency and reproducibility. Solar cells fabricated with optimized deposition achieved a record PCE of 10.7% with an FF of 79% for an area of

0.04 cm² and 9.36% for an area of 1 cm². It is important to underline that this is one of the highest efficiency values ever reported for Sn-based PSCs fabricated by a scalable technique. Additionally, solar cells retain over 90% of the initial PCE over 4 months in an inert atmosphere and degraded less than 20% after tracking the MPP for 140 h.

2. Results and Discussion

The growth of SnI₂ films is critical for the subsequent intercalation of the ammonium salts and the resulting conversion of this precursor layer into the perovskite phases in this two-step sequential deposition method.^[35] A schematic diagram of the SnI₂ film deposition procedure is presented in **Figure 1a**, to which in the following we will refer to as “first step”. The precursor solution is spread across the substrate by the blade; however, the formation of meniscus gives rise to non-classical coffee-ring-like structures during solvent evaporation. As depicted in the optical microscopy images in **Figure 1c**, a discontinuous film composed of large but isolated grains is observed, resulting from multiple factors including directional solvent evaporation, substrate interaction, and flow dynamics induced by the blade shape. This further promotes the disordered growth of perovskite grains on the SnI₂ layer, introducing undesirable nonradiative recombination sites that can severely compromise the efficiency and stability of PSCs. To optimize the crystallinity and uniformity of the SnI₂ film, we examined the influence of blade coating parameters on their nucleation and crystallization behavior, as illustrated in **Figure 1b**. Experimental details and variable controls are provided in the **Supporting Information**.

We first studied the effect of the solvent ratio (DMF: DMSO) on the SnI₂ film quality and the resulting performance of the 2D/3D PEA₂FA₄Sn₅I₁₆-based devices. DMSO, owing to its high boiling point and strong coordination ability, prolongs the solvent-complexation of the precursors within the film. This facilitates more homogeneous nucleation, slows down crystal growth, and promotes the formation of larger grains. However, the oxidation of Sn²⁺ to Sn⁴⁺ promoted by DMSO also leads to the easy formation of Sn vacancies damaging the crystallization process.^[36] In case of an excess of DMSO, it can be trapped in the film increasing Sn oxidation and giving rise to poor perovskite quality, with the presence of pinholes and isolated grains (Figure S1a, Supporting Information). Thus, achieving uniform and highly crystalline SnI₂ films requires precise regulation of the solvent ratio. Figure S2a (Supporting Information) illustrates the improved average PCE (7.56% ± 0.12%) and FF (67.50% ± 0.58%), along with a narrower distribution, achieved with a DMF:DMSO ratio of 19:1. In contrast, lower performance was observed with pure DMF due to weaker coordination and poor crystallinity, while higher DMSO ratios resulted in greater variability owing to non-uniform nucleation and crystal growth associated with solvent evaporation.^[37] Therefore, we fix the DMF:DMSO ratio to 19:1 as it minimizes the risk of Sn oxidation and ensures better crystallization during blade coating.

The growth of SnI₂ crystals and the resulting film morphology also depend on the coating temperature and speed. As shown in Figure S2b (Supporting Information), optimal performances are obtained for SnI₂ films growth at 50 °C. At low temperatures, uncontrollable solute saturation and residual solvent diffusion lead to uncontrolled nucleation and crystallization, resulting in poor film morphology and device performance (see Figures S1b and S2b, Supporting Information). In addition, the wet film may persist in a solvent-rich state for an extended period, thereby increasing the likelihood of Sn²⁺ oxidation. Fixing the optimal temperature, we further investigated the effect of coating speed on the film quality. A higher average PCE and FF were obtained using a coating speed of 10 mm s⁻¹. At a higher coating speed (e.g., 20 mm s⁻¹), the lower shear forces applied to the solution directly impact the wet film thickness, solvent evaporation rate, and the resulting SnI₂ microstructure. The nucleation and film growth are insufficient under these conditions, leading to the formation of large but isolated grains (Figure S1c, Supporting Information), this reduces the PCEs and causes significant efficiency variation, as shown in Figure S2c (Supporting Information). Therefore, we can conclude that the temperature and speed of blade coating are key parameters in achieving uniform and pinhole-free tin perovskite thin films.

The effect of the waiting time of the SnI₂ film on the hot coating stage after blade removal was also investigated, this we believe has been overlooked until now. The optical micrographs show no obvious difference under longer retention time (Figure S1d, Supporting Information); however, the atomic force microscopy (AFM) micrographs of the SnI₂ films display a rough surface (RMS of 32.73 nm) along with poor mesoporous structure for films fabricated with longer waiting time (Figure S3, Supporting Information). We propose that short delays allow partial solvent evaporation, leading to uniform films, whereas long delays promote oxidation. The statistical analysis shows that the average PCEs decreases from 7.71% ± 0.09% to 6.05% ± 0.29% as the

waiting time increased from 4 to 8 s (Figure S2d, Supporting Information). The influence of transfer time is further shown in Figure S4 (Supporting Information) and discussed in the experimental section.

Finally, efficient PEA₂FA₄Sn₅I₁₆-based devices are obtained by optimizing the nucleation and growth of SnI₂ film through control of first step processing parameters, including the DMF:DMSO ratio (19:1), coating temperature (50 °C), coating speed (10 mm s⁻¹), and waiting time (4 s). The low variation from cell to cell in the same substrate indicates a good uniformity of the film with the optimized blade coating technique (Figure S5 and Table S1, Supporting Information), which is further confirmed by the AFM morphology and roughness measured in four regions (see Figure S6, Supporting Information). To better understand the quality of SnI₂ films, X-ray diffraction (XRD) patterns are presented in Figure 1d and Figure S7 (Supporting Information). The results indicate that the preferred orientation of our films deposited with the above described optimal conditions corresponds to the (001) plane.^[35] It is interesting to note that, under optimized conditions, the diffraction patterns do not show peaks corresponding to crystalline adducts of SnI₂ with molecules of solvents. The pattern also reveals a narrow full width at half-maximum (FWHM) and strong peak intensity, confirming high crystallinity and providing favorable conditions for the subsequent interaction with ammonium salts. Notably, the higher the crystallinity of the annealed SnI₂ film, the fastest the formation of the perovskite phase.^[38] However, under unoptimized conditions, as shown in Figure S7a–c (Supporting Information), these films exhibit low diffraction intensity and broad FWHM, which we attribute to enhanced oxidation and limited solvent evaporation.

The La Mer mechanism can be applied to elucidate the different stages of SnI₂ nucleation and crystal growth from the precursor solution during the blade coating process. As demonstrated in Figure 1e, in our thermally assisted blade coating, the SnI₂ solution concentration increases until it reaches the supersaturation point (Cs), initiating the formation of nuclei (Stage I). As the concentration approaches the critical point (Cc) (Stage II), the nuclei continue to grow via solute diffusion while nucleation still occurs. When solute consumption surpasses solvent evaporation, the concentration drops below Cs, entering Stage III, where only the growth of existing nuclei proceeds without the formation of new ones.^[27] In this process, the nucleation and growth rates are strongly influenced by the solvent's evaporation rate. A low evaporation rate allows the initially formed nuclei sufficient time and space to grow into large crystals; however, it can also lead to localized solute accumulation on the substrate, resulting in SnI₂ films with poor surface coverage (see Figure 1c). In these slow-drying regimes, the dominance of diffusive over convective transport can further promote solute accumulation at local energy minimal on the substrate, such as defects or areas with surface energy variations. And the ratio of evaporation to crystallization rates emerges as the key parameter determining film morphology.^[39] Therefore, we succeed in optimizing the crystallization behavior and film uniformity of SnI₂ by modulating the nucleation and growth dynamics through controlled variations in coating speed, waiting time, processing temperature, and solvent formulation.

Regardless of the crystallinity of the SnI₂ film obtained in the first step, the second step involves the interaction of hexagonal

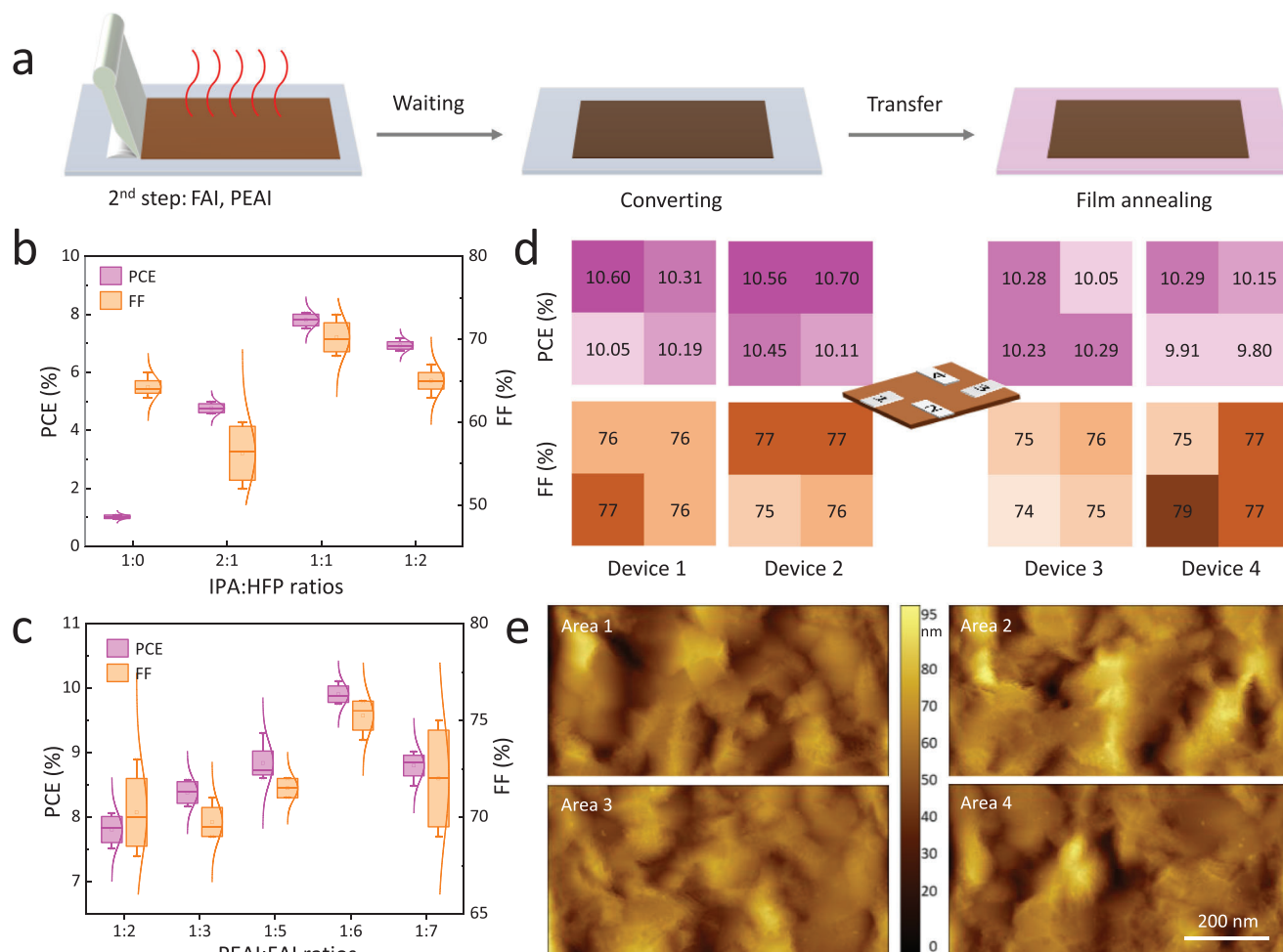


Figure 2. Impact of conversion and crystallization control in the 2nd step on device performance. a) Schematic diagram of the deposition of the ammonium salts on the surface of SnI₂ film to convert it into the perovskite phase (second step). b) Statistical distribution of PCE and FF of PEA₂FA₄Sn₅I₁₆-based devices obtained using different solvent ratios in the second step. c) Statistical distribution of PCE and FF for Sn perovskite devices fabricated with different PEAI:FAI ratios. The statistical distribution is based on 8 devices. d) The distribution of PCE and FF values for the best Sn devices in different substrate regions. e) AFM images of four different regions of a 2D/3D Sn perovskite film.

SnI₂ with ammonium salts and the subsequent conversion to the perovskite structure, which exhibits larger unit cell parameters (Figure 2a). Isopropyl alcohol (IPA) is commonly used as the solvent for ammonium salts in the second step; however, our experiments show that it does not favor the conversion and oriented crystallization of Sn-based perovskites. As shown in the XRD measurements reported in Figure S8 (Supporting Information), a weak (100) diffraction peak and the emergence of a (111) orientation are observed when pure IPA is used in the second step. In fact, as previously reported, IPA can degrade tin-based films.^[40] To overcome this issue, we introduced hexafluoro-2-propanol (HFP) as a co-solvent alongside IPA. Compared with IPA, HFP possesses a lower boiling point and a stronger electron-withdrawing capacity. In films treated with this solvent mixture during the second step, the intensity of the (100) diffraction peak is three times higher than that obtained with pure IPA (Figure S8, Supporting Information), indicating that the solvent mixture promotes the conversion to the perovskite phase. This enhancement is attributed to hydrogen bonding interactions among HFP,

IPA, and the ammonium salts. Specifically, hydrogen bonding between IPA and HFP modulates solvation dynamics, and reshapes the supersaturation profile during solvent evaporation. In addition, the electron-withdrawing nature of HFP increases solvent polarity, thereby altering the coordination dynamics between solvent molecules and the organic cation. These effects promote the formation of maximum-boiling-point complexes,^[41] which slow solvent evaporation and enhance conversion kinetics, ultimately leading to more uniform grains and complete conversion to the perovskite phase.^[40] Figure 2b demonstrated a dramatic doubling of device performance when introducing the co-solvent, with the best value obtained with a 1:1 ratio of IPA to HFP. We can therefore emphasize that the selection of solvents for the ammonium salts in the second step is as important as the one of DMF and DMSO for the first step.

Although 2D/3D PEA₂FA₄Sn₅I₁₆ perovskites (PEAI:FAI = 1:2) achieve a good PCE (>8%), a relatively weaker (100) diffraction intensity and the presence of a (111) oriented perovskite are shown by the XRD patterns (Figure S8, Supporting Information). An

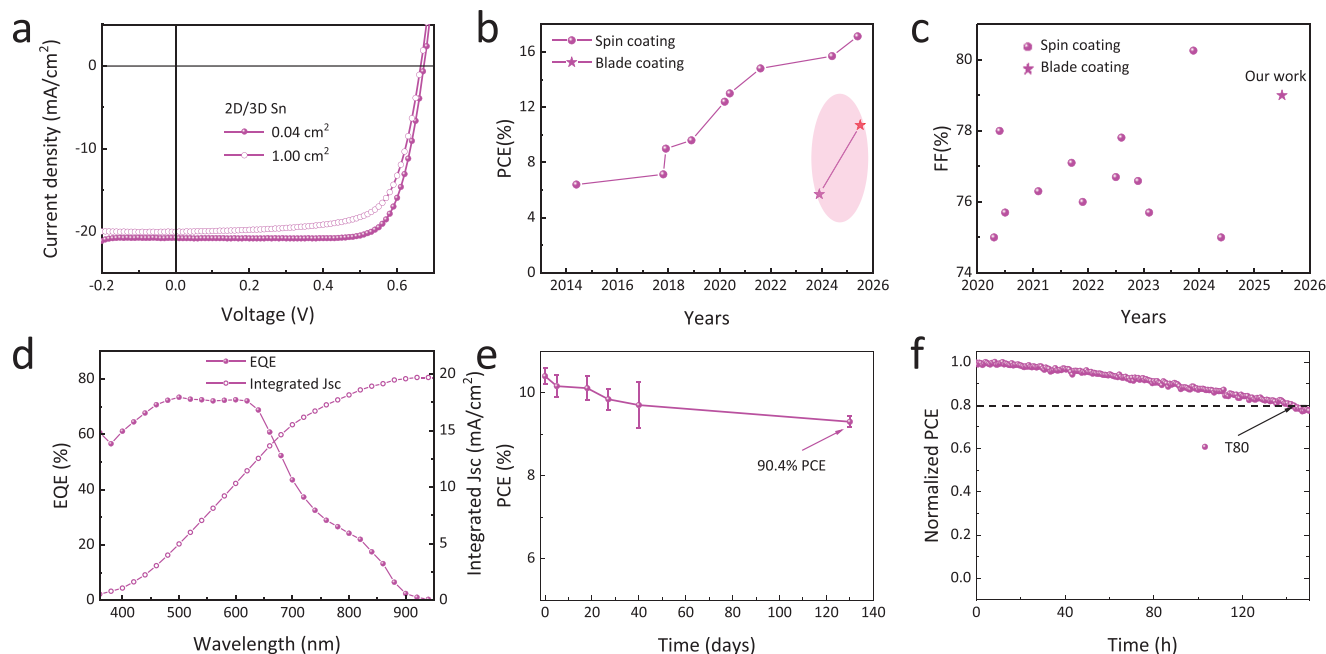


Figure 3. 2D/3D Sn device characteristics. a) J - V curves of champion 2D/3D Sn devices with areas of 0.04 and 1.00 cm². b) The PCE evolution of Sn solar cells fabricated with spin coating and blade coating (see Table S4, Supporting Information). c) Summary of the FF values of our device compared to previously reported Sn solar cells with FF greater than 75% (see Table S5, Supporting Information). d) EQE spectra and integrated photocurrent of the 2D/3D Sn device. e) Storage and f) operational stability of non-encapsulated 2D/3D devices measured in a glovebox, and MPP stability under continuous 1 sun (AM1.5G) illumination.

excessive presence of low dimensional phases, while beneficial for film stability, is detrimental to device performance as it limits the transport properties of the active layer. We therefore investigated the impact of the relative amounts of organic cations (FAI, PEAI) on device performance. In Figure 2c, we can see a clear trend with efficiency exceeding 10% and remarkably high FF at PEAI:FAI = 1:6. This excellent results are attributed to the presence of an optimal amount of 2D components, which, compared to pure 3D or quasi-2D phases, facilitate the formation of low-defect crystalline film and passivate defects at the grain boundaries.^[42,43] Unless otherwise stated, 2D/3D Sn perovskites hereafter will be based on PEAI:FAI = 1:6.

We further studied the effects of second step coating temperature, coating speed, waiting time, and transfer time on the final device performance. As shown in Table S2 (Supporting Information), the obtained optimal parameters for the second step include a solvent ratio of IPA:HFP (1:1), coating temperature of 50 °C, coating speed of 10 mm s⁻¹, and waiting time of 2 s. Higher coating speeds, lower coating temperatures, and longer waiting times significantly affect film morphology and surface coverage (Figure S9, Supporting Information), as well as diffraction intensity and FWHM (Figure S10, Supporting Information).

Thanks to the optimization of the conversion dynamics through the fine-tuning the coating parameters in both the first and second steps, we can fabricate efficient Sn-based devices in a highly reproducible way. Figure 2d and Figure S11 (Supporting Information) present the average values and standard deviations for the optimized devices: PCE = 10.269 ± 0.263%, FF = 76.125 ± 1.204%, J_{SC} = 20.646 ± 0.633 mA cm⁻², and V_{OC} = 0.654 ± 0.015 V, indicating that the devices are highly homoge-

neous. The high sample homogeneity is also confirmed by the AFM micrographs, which show the roughness of the four areas being 5.49, 5.71, 5.40, and 4.50 nm, respectively (Figure 2e).

Devices fabricated with fully optimized parameters achieved a PCE of 10.7%, a V_{OC} of 0.672 V, a J_{SC} of 20.75 mA cm⁻², and an FF of 77% (Figure 3a; Figure S13, Supporting Information), which is one of the highest efficiencies reported for tin-based devices prepared using scalable technique, as it is shown by the literature comparison reported in Figure 3b. Additionally, we also prepared devices with an area of 1 cm², achieving an efficiency of 9.36% which is only 12.5% loss compared to small-area (0.04 cm²) devices (Table S3, Supporting Information). Interestingly, the average values and standard deviations for the optimized 1 cm² devices are: PCE = 7.921% ± 0.842%, J_{SC} = 19.264 ± 0.993 mA cm⁻², V_{OC} = 0.624 ± 0.034 V, and FF = 65.75% ± 3.151%. This scalability is highly promising for the future exploitation of tin perovskite devices.

Moreover, we would like to underline the outstanding FF of 79%, as compared with recent literature data shown in Figure 3c and Figure S13 (Supporting Information), which is a signature of highly crystalline films with low defect density. The integrated J_{SC} values for the optimal device calculated from the external quantum efficiency (EQE) is 19.69 mA cm⁻² (Figure 3d), which agrees well with the value measured from the J - V curves. However, we notice that the EQE spectra show a non-ideal shape (see also the UV-vis absorption spectra in Figure S14, Supporting Information), indicating problems in extracting carriers generated with low energy photos. Moreover, the limited film thickness (≈170 nm) also results in limited light absorption at longer wavelengths. Besides efficiency, stability is equally important for

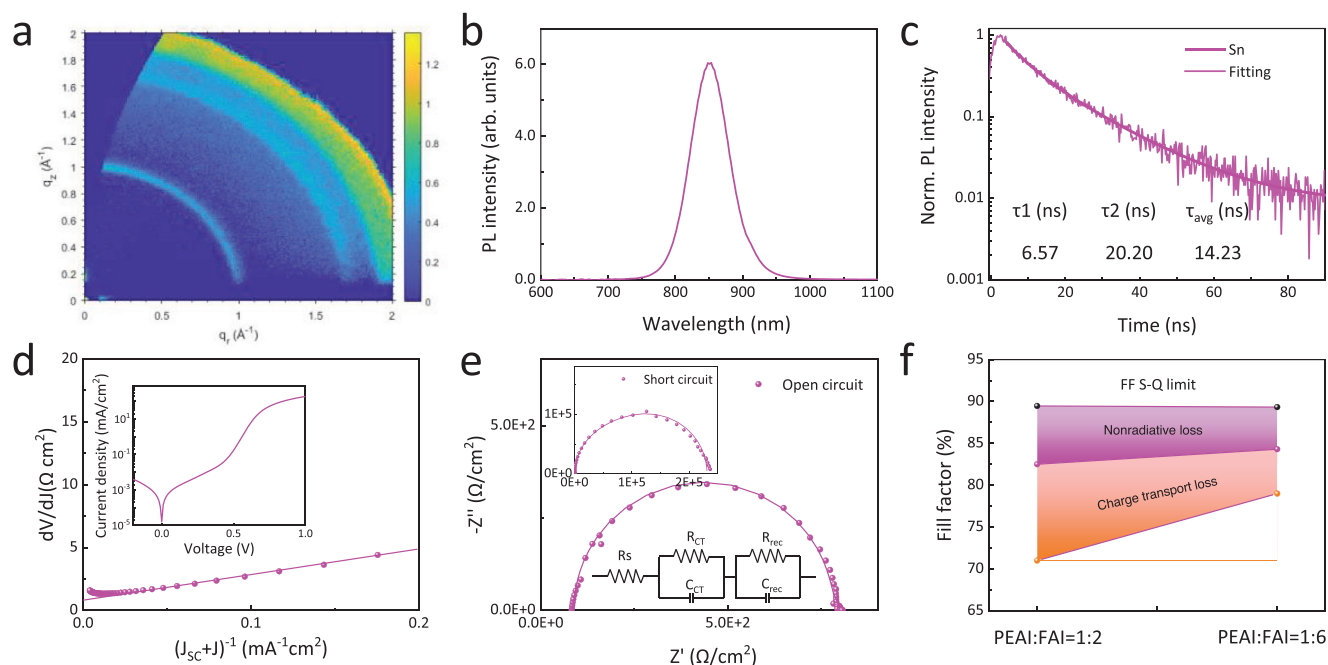


Figure 4. Electrical properties of perovskite films and devices. a) GIWAXS pattern of the 2D/3D Sn perovskite film recorded using an incident angle of 0.2° . b) Steady-state PL and c) time-resolved PL curves of the optimized 2D/3D perovskite films. d) Plot of dV/dJ versus $(J_{sc}+J)^{-1}$ (symbols) and the linear fitted curve (solid lines). The insert shows the plot of the dark current of 2D/3D Sn PSC. e) Electrochemical impedance spectra of the device measured under dark conditions at open-circuit and short-circuit states, the insert shows the equivalent circuit used for the fitting. f) The devices FF S-Q limit consists of charge-transport loss and nonradiative loss.

the practical applications of PSCs. We tracked the stability of the prepared Sn perovskite device, which maintained over 90% of its initial efficiency after up to 4 months in inert atmosphere (Figure 3e). Furthermore, the device retains $\approx 80\%$ of its efficiency after continuous operation at the maximum power point (MPP) for 140 h (Figure 3f). Therefore, we have achieved efficient tin-based devices through controlled crystallization and conversion using a scalable technique.

To clarify the reasons for the enhanced device performance discussed above, we first studied the morphology and crystallinity of 2D/3D Sn thin films by scanning electron microscopy (SEM), XRD, and Grazing-incidence wide-angle X-ray scattering (GIWAXS) measurements. As shown in Figure S15 (Supporting Information), top-view SEM images display a uniform, pinhole-free, and low defects surface morphology both in the large- and small-scale images. The optimized films show high crystallinity (Figure S16, Supporting Information), which is attributed to the better crystallinity of the SnI_2 at the first step and enhanced conversion during the second step. The GIWAXS patterns acquired using incident angles of 0.2° (surface structure) and 1.2° (bulk structure) are reported in Figures 4a and S16 (Supporting Information), respectively. The patterns revealed the presence of a 3D-like cubic (Pm-3m) structure with $a = b = c = 6.3 \text{ \AA}$, which is consistent with previously reported structures.^[44] The isotropic 3D phase shows three diffraction Debye-Scherrer rings, corresponding to the (100), (111), and (200) planes, which are visible both at the surface and in the bulk of the film. The optical properties of the films further confirm their high quality, as shown in Figure 4b, the steady-state photoluminescence (PL) spectra exhibit a sharp emission peak centered at $\approx 850 \text{ nm}$, with a full

width at FWHM of $\approx 66 \text{ nm}$. The narrow peak and high PL intensity suggest good crystallinity and low defect density.^[5,42] Also, the measured UV-vis absorption band edge is in agreement with the PL peak (Figure S14, Supporting Information). In addition, a long carrier lifetime of 14.23 ns is measured, further suggesting the low trap density of the film and the suppression of non-radiative recombination achieved with the optimized deposition strategy (Figure 4c).^[42,45,46]

Regarding the performance enhancements, which are likely due to the low defects and suppressed non-radiative recombination, there is a limited understanding about how these factors specifically contribute to the high FF achieved. Figure S17 (Supporting Information) demonstrates that the device with a lower PEAI content exhibits a lower slope of the V_{oc} versus light intensity, confirming that trap-assisted non-radiative recombination losses are better suppressed. As shown in Figure 4d and Figure S18 (Supporting Information), the $J-V$ behavior can be further analyzed using the following Equation (1):

$$\frac{dV}{dJ} = \frac{nK_B T}{q(J_{sc} + J)^{-1}} + R_s \quad (1)$$

where n , K_B , R_s , q , and T are the ideality factor, Boltzmann constant, series resistance, elementary charge, and absolute temperature, respectively.^[47] The 2D/3D Sn device (PEAI:FAI = 1:6) exhibits a lower R_s value of $0.82 \text{ } \Omega \text{ cm}^2$ compared with the 2D/3D device with PEAI:FAI = 1:2, which has an R_s value of $1.21 \text{ } \Omega \text{ cm}^2$. Similar phenomena are also observed in the dark current characteristics. This reduction is associated with an improved FF value. Electrochemical impedance spectroscopy (EIS)

also confirmed that the 2D/3D device (PEAI:FAI = 1:6) exhibits a lower charge transfer resistance (R_{CT}) and larger recombination resistance (R_{rec}),^[48] as shown in Figure 4e; Figure S19, and Table S6 (Supporting Information). These improvements are attributed to the low trap density in the corresponding perovskite films. To gain a deeper insight into the high FF, the FF loss between the Shockley-Queisser (S-Q) limit and the measured FF is investigated.^[49] The maximum FF (FF_{max}) can be calculated with the Equation (2):^[49]

$$FF_{max} = \frac{qV_{oc}/nk_B T - \ln(qV_{oc}/nk_B T + 0.72)}{qV_{oc}/nk_B T + 1} \quad (2)$$

where n , K_B , R_S , q , and T retain the same meaning as in Equation (1). As illustrated in Figure 4f, the calculated FF_{max} values are 82.5% and 84.3% for 2D/3D devices with PEAI:FAI = 1:2 and PEAI:FAI = 1:6, respectively. Trap-assisted non-radiative loss and charge transport losses are lower in 2D/3D Sn devices with a lower content of bulkier organic cations, showing both an inhibited non-radiative recombination and improved charge transport. Additionally, capacitance–voltage ($C-V$) measurements reveal charge accumulation at the interfaces, which can influence recombination and charge extraction efficiency. As shown in Figure S20 (Supporting Information), the built-in potential (V_{bi}) is 0.6 V for PEAI: FAI = 1:6 and 0.57 V for PEAI: FAI = 1:2. A higher V_{bi} facilitates more efficient charge carrier extraction, which directly contributes to higher FF and V_{OC} under illumination.^[50] Therefore, multiple measurements consistently indicate that low recombination losses and high charge transport are determining the improvement of the FF, further illustrating that the presented deposition strategy is highly promising for Sn-based perovskites.

3. Conclusion

In summary, a two-step blade coating process for efficient Sn perovskite solar cells is demonstrated for the first time. By systematically studying the parameter space of the blade coating process and its impact on the crystallization and conversion of perovskites during the first and second steps, we successfully fabricated 2D/3D Sn devices with a PCE of 10.7%. This PCE is remarkable, representing the highest reported value for these active materials deposited with scalable fabrication techniques, and is accompanied by a record FF of 79%. Additionally, our devices show excellent reproducibility and substrate uniformity. More than 90% of the PCE of these optimized devices is retained after storage in an inert atmosphere for over 4 months, and $\approx 80\%$ is maintained after MPP tracking for 140 h. Photoluminescence spectra and resistance analysis indicate that reduced non-radiative recombination and improved charge transport are key factors contributing to the high PCE and FF achieved in this study. We believe our work offers new hope for the exploitation of Sn-based PSCs using industry-compatible techniques.

Supporting Information

Supporting Information is available from the Wiley Online Library or from the author.

Acknowledgements

The work was part of the Netherlands Organization of Scientific Research (NWO) – Focus Group “Next Generation Organic Photovoltaics”, participating in the Dutch Institute for Fundamental Energy Research (DIFFER). The authors kindly acknowledge T. Zaharia and A. Kamp for technical support. L. Chen acknowledges the China Scholarship Council. The authors thank TOYOTA for financial support.

Conflict of Interest

The authors declare no conflict of interest.

Data Availability Statement

The data that support the findings of this study are available in the supplementary material of this article.

Keywords

blade coating, high fill factor, non-radiative recombination, tin perovskite

Received: July 1, 2025
Revised: September 30, 2025
Published online:

- [1] Y. Zhou, I. Poli, D. Meggiolaro, F. De Angelis, A. Petrozza, *Nat. Rev. Mater.* **2021**, *6*, 986.
- [2] J. Xi, M. A. Loi, *ACS Energy Lett.* **2021**, *6*, 1803.
- [3] K. P. Marshall, M. Walker, R. I. Walton, R. A. Hatton, *Nat. Energy* **2016**, *1*, 16178.
- [4] T. Wu, X. Liu, X. Luo, X. Lin, D. Cui, Y. Wang, H. Segawa, Y. Zhang, L. Han, *Joule* **2021**, *5*, 863.
- [5] S. Shao, J. Liu, G. Portale, H.-H. Fang, G. R. Blake, G. H. ten Brink, L. J. A. Koster, M. A. Loi, *Adv. Energy Mater.* **2018**, *8*, 1702019.
- [6] T. Wang, H. L. Loi, J. Cao, Z. Qin, Z. Guan, Y. Xu, H. Cheng, M. G. Li, C. S. Lee, X. Lu, F. Yan, *Adv. Sci.* **2022**, *9*, 2200242.
- [7] H. Zhu, W. Yang, Y. Reo, G. Zheng, S. Bai, A. Liu, Y.-Y. Noh, *Nat. Electron.* **2023**, *6*, 650.
- [8] A. Liu, H. Zhu, S. Bai, Y. Reo, T. Zou, M.-G. Kim, Y.-Y. Noh, *Nat. Electron.* **2022**, *5*, 78.
- [9] X. Jiang, H. Li, Q. Zhou, Q. Wei, M. Wei, L. Jiang, Z. Wang, Z. Peng, F. Wang, Z. Zang, K. Xu, Y. Hou, S. Teale, W. Zhou, R. Si, X. Gao, E. H. Sargent, Z. Ning, *J. Am. Chem. Soc.* **2021**, *143*, 10970.
- [10] B. B. Yu, Z. Chen, Y. Zhu, Y. Wang, B. Han, G. Chen, X. Zhang, Z. Du, Z. He, *Adv. Mater.* **2021**, *33*, 2102055.
- [11] C. Ran, J. Xi, W. Gao, F. Yuan, T. Lei, B. Jiao, X. Hou, Z. Wu, *ACS Energy Lett.* **2018**, *3*, 713.
- [12] Z. Zhang, Y. Huang, C. Wang, Y. Jiang, J. Jin, J. Xu, Z. Li, Z. Su, Q. Zhou, J. Zhu, R. He, D. Hou, H. Lai, S. Ren, C. Chen, X. Gao, T. Shi, W. Hu, F. Fu, P. Gao, D. Zhao, *Energy Environ. Sci.* **2023**, *16*, 3430.
- [13] K. Nishimura, M. A. Kamarudin, D. Hirotoni, K. Hamada, Q. Shen, S. Iikubo, T. Minemoto, K. Yoshino, S. Hayase, *Nano Energy* **2020**, *74*, 104858.
- [14] Y. Su, J. Yang, H. Rao, Y. Zhong, W. Sheng, L. Tan, Y. Chen, *Energy Environ. Sci.* **2023**, *16*, 2177.
- [15] G. Li, Z. Su, M. Li, F. Yang, M. H. Aldamasy, J. Pascual, F. Yang, H. Liu, W. Zuo, D. Di Girolamo, Z. Iqbal, G. Nasti, A. Dallmann, X. Gao, Z. Wang, M. Saliba, A. Abate, *Adv. Energy Mater.* **2021**, *11*, 2101539.
- [16] C.-H. Kuan, J.-M. Chih, Y.-C. Chen, B.-H. Liu, C.-H. Wang, C.-H. Hou, J.-J. Shyue, E. W.-G. Diau, *ACS Energy Lett.* **2022**, *7*, 4436.

- [17] C. Wang, F. Gu, Z. Zhao, H. Rao, Y. Qiu, Z. Cai, G. Zhan, X. Li, B. Sun, X. Yu, B. Zhao, Z. Liu, Z. Bian, C. Huang, *Adv. Mater.* **2020**, *32*, 1907623.
- [18] M. Pitaro, E. K. Tekelenburg, S. Shao, M. A. Loi, *Adv. Mater.* **2022**, *34*, 2105844.
- [19] Y. Shi, Z. Zhu, D. Miao, Y. Ding, Q. Mi, *ACS Energy Lett.* **2024**, *9*, 1895.
- [20] D. He, P. Chen, J. A. Steele, Z. Wang, H. Xu, M. Zhang, S. Ding, C. Zhang, T. Lin, F. Kremer, H. Xu, M. Hao, L. Wang, *Nat. Nanotechnol.* **2025**, *20*, 779.
- [21] J. Cao, F. Yan, *Energy Environ. Sci.* **2021**, *14*, 1286.
- [22] X. Jiang, F. Wang, Q. Wei, H. Li, Y. Shang, W. Zhou, C. Wang, P. Cheng, Q. Chen, L. Chen, Z. Ning, *Nat. Commun.* **2020**, *11*, 1245.
- [23] X. Liu, Y. Wang, T. Wu, X. He, X. Meng, J. Barbaud, H. Chen, H. Segawa, X. Yang, L. Han, *Nat. Commun.* **2020**, *11*, 2678.
- [24] Y. Xiao, C. Zuo, J. X. Zhong, W. Q. Wu, L. Shen, L. Ding, *Adv. Energy Mater.* **2021**, *11*, 2100378.
- [25] W. Zuraw, F. A. Vinocour Pacheco, J. Sanchez-Diaz, L. Przypis, M. A. Mejia Escobar, S. Almosni, G. Vescio, J. P. Martinez-Pastor, B. Garrido, R. Kudrawiec, I. Mora-Sero, S. Oz, *ACS Energy Lett.* **2023**, *8*, 4885.
- [26] X. Liu, T. Wu, X. Luo, H. Wang, M. Furue, T. Bessho, Y. Zhang, J. Nakazaki, H. Segawa, L. Han, *ACS Energy Lett.* **2021**, *7*, 425.
- [27] J. W. Lee, D. K. Lee, D. N. Jeong, N. G. Park, *Adv. Funct. Mater.* **2018**, *29*, 1807047.
- [28] L. Chen, F. Tavormina, L. D. Mario, M. Pitaro, G. Portale, N. Masciocchi, A. Guagliardi, M. A. Loi, *Adv. Energy Mater.* **2025**, 2405941.
- [29] P. Wang, Y. Wu, B. Cai, Q. Ma, X. Zheng, W. H. Zhang, *Adv. Funct. Mater.* **2019**, *29*, 1807661.
- [30] L. Chen, S. Saleh, F. Tavormina, L. Di Mario, J. Li, Z. Xie, N. Masciocchi, C. J. Brabec, B. Koldehofe, M. A. Loi, *Adv. Mater.* **2025**, *37*, 2414430.
- [31] Z. Wu, E. Bi, C. Li, L. Chen, Z. Song, Y. Yan, *Sol. RRL* **2023**, *7*, 2200571.
- [32] J. Zhang, T. Bu, J. Li, H. Li, Y. Mo, Z. Wu, Y. Liu, X.-L. Zhang, Y.-B. Cheng, F. Huang, *J. Mater. Chem. A* **2020**, *8*, 8447.
- [33] L. Chen, E. K. Tekelenburg, K. Gahlot, M. Pitaro, J. Xi, A. Lasorsa, G. Feraco, L. Protesescu, P. C. A. van der Wel, G. Portale, P. Rudolf, C. J. Brabec, M. A. Loi, *Energy Environ. Sci.* **2023**, *16*, 5315.
- [34] J. Liu, H. Yao, S. Wang, C. Wu, L. Ding, F. Hao, *Adv. Energy Mater.* **2023**, *13*, 2300696.
- [35] W. Shao, H. Wang, F. Ye, C. Wang, C. Wang, H. Cui, K. Dong, Y. Ge, T. Wang, W. Ke, G. Fang, *Energy Environ. Sci.* **2023**, *16*, 252.
- [36] A. Abate, *ACS Energy Lett.* **2023**, *8*, 1896.
- [37] L. Chao, T. Niu, W. Gao, C. Ran, L. Song, Y. Chen, W. Huang, *Adv. Mater.* **2021**, *33*, 2005410.
- [38] A. Ummadisingu, L. Steier, J. Y. Seo, T. Matsui, A. Abate, W. Tress, M. Gratzel, *Nature* **2017**, *545*, 208.
- [39] M. Majewski, S. Qiu, O. Ronsin, L. Luer, V. M. Le Corre, T. Du, C. J. Brabec, H. J. Egelhaaf, J. Harting, *Mater. Horiz.* **2025**, *12*, 555.
- [40] S. Shahbazi, M.-Y. Li, A. Fathi, E. W.-G. Diau, *ACS Energy Lett.* **2020**, *5*, 2508.
- [41] J. A. Floria, U.S. Patent **1972**, *3*, 691, 092.
- [42] L. J. M. van de Ven, E. K. Tekelenburg, M. Pitaro, J. Pinna, M. A. Loi, *ACS Energy Lett.* **2024**, *9*, 992.
- [43] C. Sun, P. Yang, Z. Nan, C. Tian, Y. Cai, J. Chen, F. Qi, H. Tian, L. Xie, L. Meng, Z. Wei, *Adv. Mater.* **2023**, *35*, 2205603.
- [44] E. C. Schueller, G. Laurita, D. H. Fabini, C. C. Stoumpos, M. G. Kanatzidis, R. Seshadri, *Inorg. Chem.* **2018**, *57*, 695.
- [45] G. Liu, Y. Zhong, W. Feng, M. Yang, G. Yang, J. X. Zhong, T. Tian, J. B. Luo, J. Tao, S. Yang, X. D. Wang, L. Tan, Y. Chen, W. Q. Wu, *Angew. Chem.* **2022**, *61*, 202209464.
- [46] J. Sanchez-Diaz, R. S. Sanchez, S. Masi, M. Krecmarova, A. O. Alvarez, E. M. Barea, J. Rodriguez-Romero, V. S. Chirvony, J. F. Sanchez-Royo, J. P. Martinez-Pastor, I. Mora-Sero, *Joule* **2022**, *6*, 861.
- [47] W. Ke, C. C. Stoumpos, I. Spanopoulos, M. Chen, M. R. Wasielewski, M. G. Kanatzidis, *ACS Energy Lett.* **2018**, *3*, 1470.
- [48] T. Li, Z. Zhang, F. He, L. Deng, Y. Yang, X. Mo, Y. Zhan, J. Liang, *Adv. Funct. Mater.* **2023**, *33*, 2308457.
- [49] C. Qi, L. Yongjiang, Z. Hong, Y. Jiabao, H. Jian, X. Ting, W. Shuangjie, W. Zishuai, G. Bingyu, Z. Junsong, L. Xiaoqiang, M. Xiaoyan, Z. S. Mohammed, S. W. E. I., L. X. Li, G. Michael, *Sci. Adv.* **2021**, *7*, abg0633.
- [50] K. Zhang, A. Späth, O. Almora, V. M. Le Corre, J. Wortmann, J. Zhang, Z. Xie, A. Barabash, M. S. Hammer, T. Heumüller, J. Min, R. Fink, L. Luer, N. Li, C. J. Brabec, *ACS Energy Lett.* **2022**, *7*, 3235.